separations

MDPI

Article

Visible Light-Assisted Periodate Activation Using Carbon Nitride for the Efficient Elimination of Acid Orange 7

Wenjun Xu [1], Qianyi Wang [1], Jintao He [1], Fuzhen Liu [2,*], Xiang Yan [3] and Yin Xu [1,*]

[1] Hubei Key Laboratory of Regional Development and Environmental Response, Faculty of Resources and Environmental Science, Hubei University, Wuhan 430062, China; x1109_123@163.com (W.X.); wangqianyi1123@163.com (Q.W.); hejintaohubu@163.com (J.H.)
[2] College of Chemistry and Chemical Engineering, Huanggang Normal University, Huanggang 438000, China
[3] Instituto de Micro y Nanotecnología, IMN-CNM, CSIC, CEI UAM + CSIC, Isaac Newton 8, Tres Cantos, E-28706 Madrid, Spain; xiang.yan@csic.es
* Correspondence: liufuzhen_lfz@163.com (F.L.); yxu@hubu.edu.cn (Y.X.)

Abstract: The development of appropriate and effective periodate (PI) activation technology is currently a popular research area. This study presents a novel efficient photocatalytic activation approach of PI for pollutant degradation based on carbon nitride (g-C_3N_4) and visible light (Vis). The results show that the system can remove 92.3% of acid orange 7 (AO7) within 60 min under the g-C_3N_4/PI/Vis reaction system. The degradation rate constant (k_{obs}) reached 4.08 × 10^{-2} min^{-1}, which is 4.21, 5.16 times, and 51.3 times higher than that of the g-C_3N_4/Vis system (9.7 × 10^{-3} min^{-1}), PI/Vis system (7.9 × 10^{-3} min^{-1}) and the g-C_3N_4/PI system (7.96 × 10^{-4} min^{-1}), respectively. Clearly, the addition of PI significantly enhances the degradation efficiency of AO7 in the system. Additionally, under the same reaction conditions, the presence of PI showed excellent oxidation capacity in the photoactivation process compared with other common oxidants, such as peroxymonosulfate, peroxydisulfate, and H_2O_2. Moreover, the g-C_3N_4/PI/Vis system showed excellent removal of AO7 across a wide range of pH levels and in the presence of various anions. Electron paramagnetic resonance (EPR) and quenching experiments suggested that the superoxide anions ($^{\bullet}O_2^-$) and singlet oxygen ($^1O_2$) dominated in the oxidation of pollutants in the g-C_3N_4/PI/Vis system. In addition, the catalyst showed relative stability during cyclic testing, although a slight reduction in degradation efficiency was observed. In brief, the g-C_3N_4/PI/Vis system is highly efficient and environmentally friendly, with significant application potential in wastewater treatment.

Keywords: carbon nitride; periodate; visible light; catalytic degradation; mechanism

Citation: Xu, W.; Wang, Q.; He, J.; Liu, F.; Yan, X.; Xu, Y. Visible Light-Assisted Periodate Activation Using Carbon Nitride for the Efficient Elimination of Acid Orange 7. *Separations* **2024**, *11*, 274. https://doi.org/10.3390/separations11090274

Academic Editor: Ki Hyun Kim

Received: 24 July 2024
Revised: 5 September 2024
Accepted: 13 September 2024
Published: 19 September 2024

1. Introduction

Over the past decade, water pollution has emerged as a significant issue, particularly due to persistent organic contaminants in water that seriously endanger both ecological and human health [1–4]. For instance, Acid Orange 7 (AO7) is a characteristic azo dye that is widely used in wool textile dyeing. This kind of azo dye is mostly resistant to biodegradation and seriously harms the ecological environment. Thus, AO7 has always been selected as a model target molecule in the water treatment filed since it contains the "core structure" of all azo dyes and possesses similar physicochemical properties [5]. To address the escalating challenge posed by refractory organics, the development of efficient and green water treatment technologies is urgently needed. Advanced oxidation processes (AOPs), based on the activation of various oxidants, are particularly effective at degrading non-biodegradable and hazardous substances, such as pesticides, pharmaceuticals, and industrial dyes. Since a sole oxidant cannot directly destroy organic contaminants due to its low redox capacity, catalysts are always required to activate oxidants (e.g., hydrogen peroxide (H_2O_2), persulfates (PS), periodate (PI), etc.) to produce highly reactive oxygen species that are able to directly degrade organic contaminants. As a result, finding an

effective catalyst that can activate an appropriate oxidant has become a research frontier [6]. Due to its easier activation and its ability to produce a variety of robust oxidative species in situ, such as superoxide radicals ($^{\bullet}O_2^-$), singlet oxygen ($^1O_2$), hydroxyl radicals ($^{\bullet}OH$), and iodine radicals ($IO_3^{\bullet}$), PI activation systems have shown great promise as rapid pollutant decontamination techniques in comparison to other common oxidants [7,8]. Despite its powerful oxidizing capacity (+1.6 V), PI struggles to efficiently eliminate organic pollutants [9]. To enhance the oxidation capacity of the system, PI has been activated using a variety of techniques, such as ultrasound (US) [10], freezing [11], alkaline [12], hydroxylamine [13], transition metals [14], and carbon-based catalysts [15]. These techniques produce a variety of reactive species that contribute to the degradation of organic contaminants in PI-based AOPs. Transition metal-based heterogeneous catalysts stand out among the numerous PI activation techniques that have been thoroughly studied because of their advantages, which include no additional energy input, low cost, ease of operation, and moderate conditions [16]. For example, metal oxides, such as MnO_2, Fe_2O_3, and Co_3O_4, have been widely used in the heterogeneous activation of PI systems, leading to the production of reactive species for rapidly degrading contaminants in water [17–19]. However, the potential for secondary contamination, induced by metal ion leaching under certain reaction conditions [20,21], hinders their widespread applications and necessitates further attention. As a result, finding highly active and environmentally friendly heterogeneous activators is critical to enhancing the practicality of this technology. In recent years, carbon materials have emerged as the most promising heterogeneous activators of peroxides for sewage treatment due to their superior activation performance and cost-effectiveness [22].

Carbon materials are gaining prominence due to their distinct characteristics, such as low cost, non-toxicity, and feasibility in synthesis and modification. A variety of carbon catalysts, including activated carbon, biochar, carbon nanotubes, and graphene, are used extensively. Chen et al. [23] reported a novel system for activating PI via metal-free polymeric carbon nitride (CN); however, it achieves a pollutant removal of only about 20% when both PI and the catalyst are present. He et al. [24] reported a novel system for activating PI via biochar prepared from pulp sludge; The complete degradation of pollutants requires 90 min, and a substantial amount of PI is needed for each group of degradation experiments. Obviously, the potential oxidation activity of PI cannot be realized unless it is effectively activated. Thus, researchers have developed a carbon material that harnesses visible light for photocatalytic degradation, promoting the oxidation process and more effectively utilizing the solar spectrum [25]. Thus, developing an appropriate carbon-based material responsive to visible light is expected to be an effective approach for PI activation.

Carbon nitride (g-C_3N_4) has received considerable interest in photocatalytic processes due to its relatively narrow band gap (~2.7 eV), facilitating efficient utilization of visible light. Furthermore, compared with other carbon materials, g-C_3N_4 stands out and exhibits advantageous characteristics, including consistent physical and chemical properties, simplicity in preparation, eco-friendliness, and the capacity for large-scale production [26,27]. Given these merits, it has been widely applied in the activation of common oxidants for the degradation of pollutants [28]. Consequently, introducing carbon nitride materials into the photoactivated PI system can greatly increase the removal efficiency of pollutants. Of note, the photoactivated PI in the presence of g-C_3N_4 system is rarely reported, and the specific reaction mechanism of the g-C_3N_4/PI/Vis ternary system deserves to be thoroughly investigated.

In this study, g-C_3N_4 was synthesized via a one-step thermal polymerization process and applied in PI activation for the elimination of AO7 under visible light irradiation. The main contents of this study are as follow: (i) investigating the ability of the g-C_3N_4/PI/Vis system to degrade AO7 and explaining the synergistic performance of the heterogeneous photocatalytic PI process; (ii) assessing the effects of catalyst dosage, PI dose, pH, and common anions on pollutant removal; (iii) exploring the dominant reactive species involved in the oxidation of contaminants and the associated activation mechanisms; (iv) evaluating the cycling capabilities of the catalyst and comparing the performance of contaminant

removal using other oxidants, such as peroxymonosulfate (PMS), peroxydisulfate (PDS), and H_2O_2. The findings of this study offer an experimental foundation and insights for the application of heterogeneous PI-activated systems in environmental remediation.

2. Materials and Methods

2.1. Chemicals and Reagents

Acid Orange 7 (≥99.0%), sodium periodate (≥99.0%), melamine (≥99.0%), and 5,5-dimethyl-1-pyrrolineoxide (DMPO, ≥97%) were purchased from Aladdin Industrial Corporation, Shanghai, China. Tertiary butanol (TBA, ≥99.5%), *p*-benzoquinone (*p*-BQ, ≥98.0%), L-histidine (≥99.5%), dimethyl sulfoxide (DMSO, ≥99.5%), potassium chloride (KCl, ≥99.5%), potassium dihydrogen phosphate (KH_2PO_4, ≥99.5%), sodium bicarbonate ($NaHCO_3$, ≥99.5%), and 2,2,6,6-tetramethyl-4-piperidone (TEMP, ≥99.0%) were purchased from Sinopharm Chemical Reagent Co., Ltd. (52, Ningbo Road, Shanghai, China).

2.2. Catalyst Preparation

Graphite phase carbon nitride (g-C_3N_4, CN) was synthesized using a simple thermal polymerization method. Firstly, 12.0 g of melamine was placed into a ceramic crucible with a lid. The crucible was heated in a furnace at a rate of 3.85 °C/min in an air atmosphere until it reached 550 °C [29,30]. After maintaining this temperature for 6 h, a light-yellow sample of CN was obtained.

2.3. Experimental Procedures

Degradation tests were conducted in a 100 mL beaker with stirring at 450 rpm and illumination from a 400 W xenon lamp (DY 400G, Guangzhou Xingchuang Electronics Co., Ltd., Guangzhou, China) equipped with a filter greater than 420 nm to filter out the ultraviolet light. The temperature was maintained at 24 ± 2 °C using a thermostatic bath in a double-layer beaker. The double-layer beaker kept the reaction temperature stable by flowing water at a constant temperature (pump circulation). The vertical distance between the xenon lamp and the reactor was 20 cm. Sodium periodate and g-C_3N_4 were added into the solution in sequence, quickly followed by illumination from a xenon lamp to initiate the reaction. The initial pH was adjusted with dilute H_2SO_4 and NaOH solutions. During the experiments, a 3 mL sample was taken at a preset time and filtered through a 0.22 μm membrane filter for immediate analysis. After the reaction, the catalyst was obtained by vacuum filtration, rinsed with ultrapure water, and dried at 80 °C overnight for later reuse and characterization.

2.4. Methods of Analysis

The absorbance of AO7 samples at 485 nm was determined using a UV-visible spectrophotometer, and the standard curve method was applied to calculate the AO7 removal rate (η), as described in Equation (1) [31].

$$\eta = (1 - C_t/C_0) \times 100\% \quad (1)$$

$$\ln(C_t/C_0) = -k_{obs} \times t \quad (2)$$

where C_t (mg/L) is the concentration of AO7 at a specific time t and C_0 (mg/L) is the initial concentration of AO7. The degradation of AO7 obeyed pseudo-first-order kinetics, which can be defined by Equation (2) [32]; k_{obs} (min^{-1}) is the pseudo-first-order rate constant and t (min) is the reaction time.

2.5. Characterization

The structural features of the sample were analyzed using an X-ray diffraction instrument (XRD, MiniFlex 600, Rigaku, Tokyo, Japan). The X-ray source was Cu Kα radiation, the wavelength was 1.5406 Å, the scanning speed was 10°/min, and the 2θ range was from 10 to 90°. The morphological characteristics were observed using field emission

scanning electron microscopy (FESEM, SIGMA 500, Steinheim, Germany). The Thermo Scientific ESCAlab 250xi spectrometer (St. Bend, OR, USA) with monochromatic Al Kα radiation was employed to obtain X-ray photoelectron spectroscopy (XPS). The tube voltage, current, and energy of the X-ray was 15 kV, 10 mA, and 1486.6 eV, respectively. The binding energies were calibrated with adventitious C1 s (284.8 eV). Electron Paramagnetic Resonance (EPR) spectra were obtained using a Bruker EMX plus spectrometer (Karlsruhe, Germany) to find reactive species that were formed during the process of oxidation, utilizing 2,2,6,6-tetramethyl-4-piperidone (TEMP) or 5,5-dimethyl-1-pyrrolineoxide (DMPO) as spin-trapping agents. For the EPR analysis, the amount of catalyst was 0.50 g/L. The amount of spin-trapping agent used was 20 µL of pure DMPO per 400 µL reaction solution and 500 µL of TEMP (50 mM) per 200 µL reaction solution, respectively. The EPR experiments were performed in a 250 mL beaker containing 100 mL of pure water (or 100 mL of anhydrous methanol or DMSO solution). Typically, 0.5 g/L g-C_3N_4 and 0.25 mM PI were uniformly dissolved in the solution, and the xenon lamp was then turned on for irradiation. After 5 min of reaction, a 400 µL sample was taken using a pipette gun and 20 µL of DMPO (or a 200 µL sample with 500 µL TEMP) was added for immediate analysis. The EPR spectra were collected under the following conditions: a center field of 3493 G, a sweep width of 100 G, a static field of 3442 G, a microwave power of 2.14 mW, a microwave frequency of 9.79 GHz, a modulation frequency of 100 kHz, a modulation amplitude of 1.0 G, and a sweep time of 30 s. UV-Vis diffuse reflectance spectroscopy (DRS) measurements were conducted using a Shimadzu UV3600 spectrometer at an excitation wavelength of 352 nm and a scanning wavelength range of 300–700 nm. Photoluminescence spectra (PL) were measured at an excitation wavelength of 250 nm (xenon lamp) using a Hitachi F7100 spectrometer (Tokyo, Japan) with a fluorescence range of 200–800 nm. The Brunauer–Emmett−Teller (BET) surface area was assessed using a N_2 adsorption–desorption isotherm analyzer apparatus (ASAP2020 Version 4.03, Micromeritics Co., Norcross, GA, USA).

3. Results and Discussion

3.1. Characterization of CN

The XRD patterns (Figure 1a) confirmed the successful preparation of pure CN and they were well matched with the standard (ICDD PDF# 87−1526) [23]. This suggests that the structural units of the sample were primarily tri-s-triazine (heptazine) rings. A strong peak (002) appeared near 27.5°, corresponding to the characteristic interplanar packing peak of the conjugated aromatic structure, whereas the appearance of another distinct peak (100) at 13.0° may be due to the in-plane structural packing motif. This confirms that CN possesses a graphitic layer structure. As is well-known, the light-harvesting ability and carrier separation of a photocatalyst affect its oxidation performance [33]. Thus, the UV-visible diffuse reflectance spectrum (UV-vis DRS) was employed to confirm the light absorption properties of CN. As shown in Figure 1b, the sample's absorption intensity and range from ultraviolet to visible light are depicted. The light absorption edge of CN was at 465 nm, indicating its capability to absorb visible light. The optical properties of the CN photocatalyst were measured using UV-Vis DRS. It can be seen that pure CN exhibits good application potential for visible-light photocatalysis. The optical band gap energy (E_g) of CN was determined using the Kubelka–Munk equation (Equation (3)) and the Tauc relationship (Equation (4)) [34].

$$F(R) = (1 - R)^2/2R \quad (3)$$

$$(\alpha h\nu)^2 = A\,(h\nu - E_g) \quad (4)$$

where R is the reflectance, F(R) is the transformed reflectance according to Kubelka–Munk, $h\nu$ is the photon energy in eV, A is a material constant, and α is the absorption coefficient, which is equivalent to F(R).

According to the Tauc method (Figure 1b), the band gap energy (E_g) of CN was determined as 2.72 eV. An absolute electronegativity approach was then applied to determine

the energy band position of the catalyst. In Equations (5) and (6), χ and E_e^- are the absolute electronegativities of a semiconductor and the electron energy (4.50 eV), respectively, whereas E_g, E_{VB}, and E_{CB} represent the energies of the band gap, valence band, and conduction band, respectively [35]. Based on previous literature [36], the absolute electronegativity for CN was determined to be 4.73 eV, resulting in an E_{VB} of 1.59 eV and an E_{CB} of −1.13 eV for CN.

$$E_{VB} = \chi - E_e^- + 1/2\, E_g \quad (5)$$

$$E_{CB} = \chi - E_e^- - 1/2\, E_g \quad (6)$$

The SEM image of CN (Figure 2a–d) reveals that it typically has a large block shape with a loose and porous structure, along with a visible layered folding structure. This structure is likely due to the significant amount of gas released by the precursor melamine during the pyrolysis process, which promotes peeling of the carbon layers [23]. The resulting thin and porous layers increase the specific surface area of the sample, enhancing its role in the degradation process. The results show that CN exhibited a classical IV isotherm and the specific surface area was 32.28 m^2/g, with a pore volume of 0.11 cm^3/g (Figure 2e). Compared to the other carbon materials listed in Table 1, CN is assumed to be conducive to the catalytic reaction due to its large surface area and pore volume (Table 1).

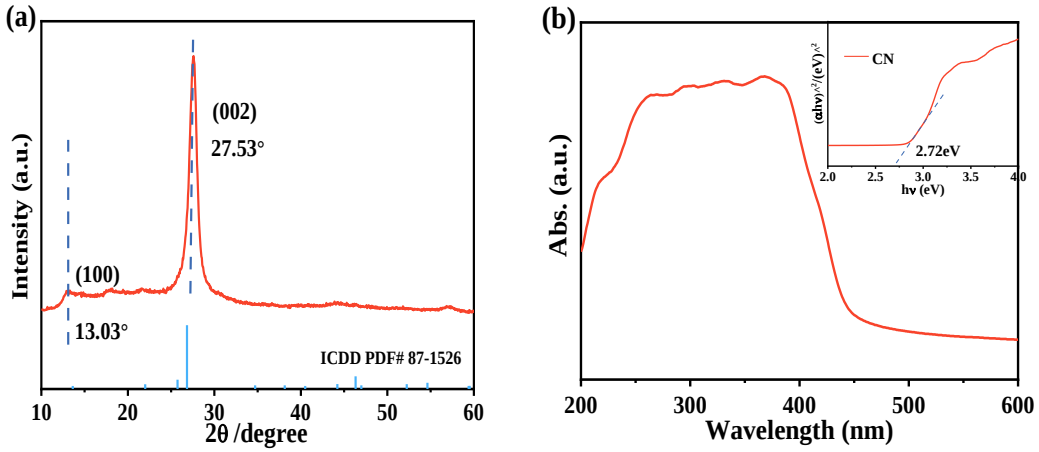

Figure 1. XRD pattern (**a**) and UV-vis absorption spectrum (**b**) of the CN sample. The inset shows the band gap of CN.

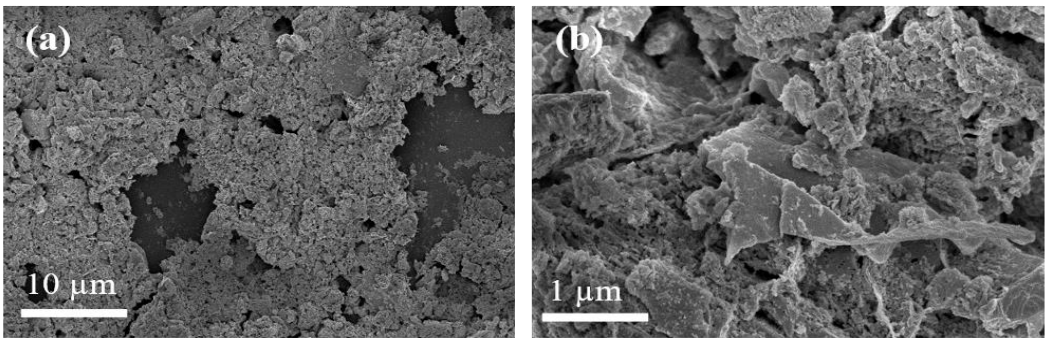

Figure 2. *Cont.*

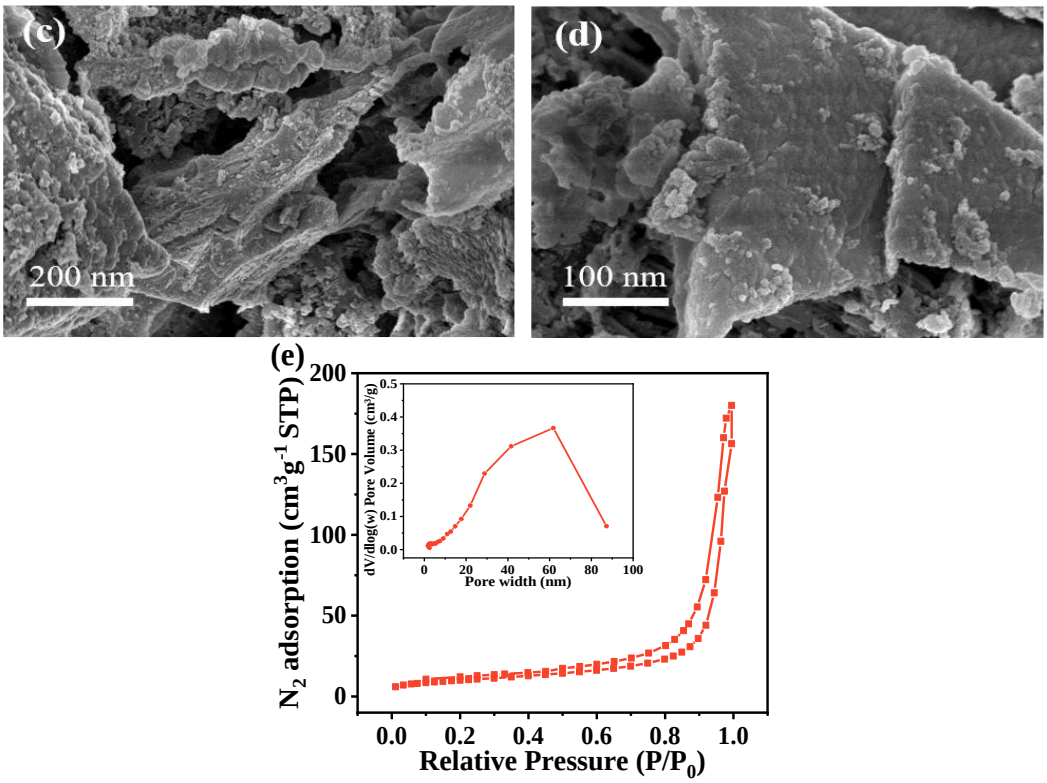

Figure 2. (**a**–**d**) SEM images of CN; (**e**) N_2 adsorption-desorption isotherms of CN. The inset shows the corresponding pore size distribution.

Table 1. Comparison of CN with other similar carbon materials.

Samples	S_{BET} (m^2/g)	Pore Volume (cm^3/g)	Ref.
CN	32.28	0.11	This work
MCN	6.18	0.003	[23]
CN-bulk	22.41	0.12	[37]
PCN	26.04	/	[38]
$C_{1.0}$CN	32.1	/	[39]

3.2. PI Activation Systems for AO7 Removal

The efficiency of AO7 removal in different systems is shown in Figure 3a. It was observed that AO7 adsorption by CN and its removal in the CN/PI process were minimal, and the sole PI/Vis system was also not able to efficiently remove AO7 [24]. Similarly, AO7 degradation was inefficient in the CN/Vis system, which might be due to the rapid recombination of photogenerated electron−hole pairs, resulting in only a trace amount of reactive substances being produced. Surprisingly, the CN/PI/Vis system degraded 92.3% of AO7 within 60 min, far surpassing the performance of other oxidation systems. Kinetic fitting revealed that AO7 removal during the oxidation process followed a pseudo-first-order model. As shown in Figure 3b, the AO7 removal rate by the CN/PI/Vis system was significantly higher than that of the CN/Vis and PI/Vis systems. The removal rate (k_{obs} = 0.0408 min^{-1}) of AO7 in the CN/PI/Vis system was 4.21 and 5.16 times higher than that in the CN/Vis (k_{obs} = 0.0097 min^{-1}) and PI/Vis (k_{obs} = 0.0079 min^{-1}) systems, respectively. These results indicate a strong synergistic effect between CN and PI in the presence of Vis for the degradation of AO7, significantly enhancing the system's activity.

To investigate electron transfer and verify the synergistic effect of PI on the photocatalysis process, photoluminescence measurements (Figure 3c) were conducted on CN and CN/PI with excitation at 350 nm. The PL intensity of the CN/PI system was very low compared with the CN sample, implying that the introduction of PI significantly inhibits charge carrier recombination and accelerates the separation of internal charges [23].

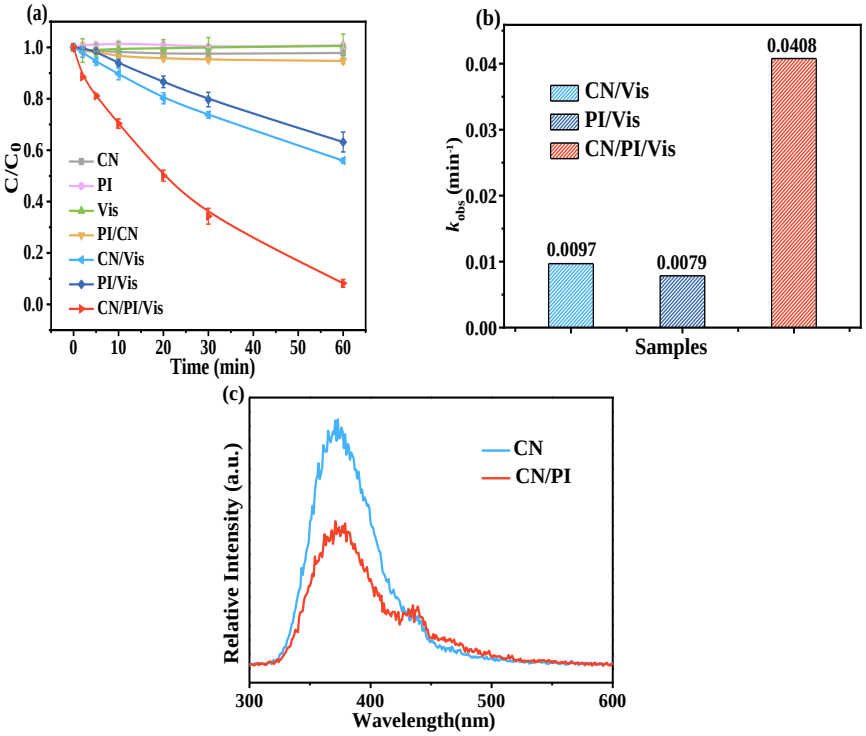

Figure 3. (**a**) Removal of AO7 and (**b**) rate constants of AO7 removal in different systems; (**c**) photoluminescence spectra of the CN and CN/PI systems. Experimental conditions: $[AO7]_0$ = 10 ppm, $[CN]_0$ = 0.50 g/L, $[PI]_0$ = 0.25 mM, and initial pH = 5.5.

Experiments on AO7 removal were also conducted to assess the photocatalytic efficiency of CN with other common oxidants, such as PMS, PDS, and H_2O_2 (Figure 4a). Under the same conditions, the photocatalytic oxidation capacity of CN with different oxidants ranks as follows: PI > PDS > PMS > H_2O_2 (Figure 4b), demonstrating the excellent ability of periodate to inhibit electron−hole pairs [40]. Compared with other oxidants, such as the PDS molecule ($d_{(O-O)}$ = 1.497 Å) and the PMS molecule ($d_{(O-O)}$ = 1.453 Å) [41], IO_4^- has a longer I-O bond ($d_{(I-O)}$ = 1.78 Å) [42]; therefore, it is more easily activated and cleaved to produce highly reactive substances. Moreover, as shown in Table 2, compared with previous literature, the CN/PI/Vis system demonstrates high performance in organic pollutant elimination, which is comparable to or even better than most similar systems reported (Table 2). Importantly, compared with other carbon materials, CN stands out due to its simplicity in preparation, eco-friendliness, and the potential for large-scale production.

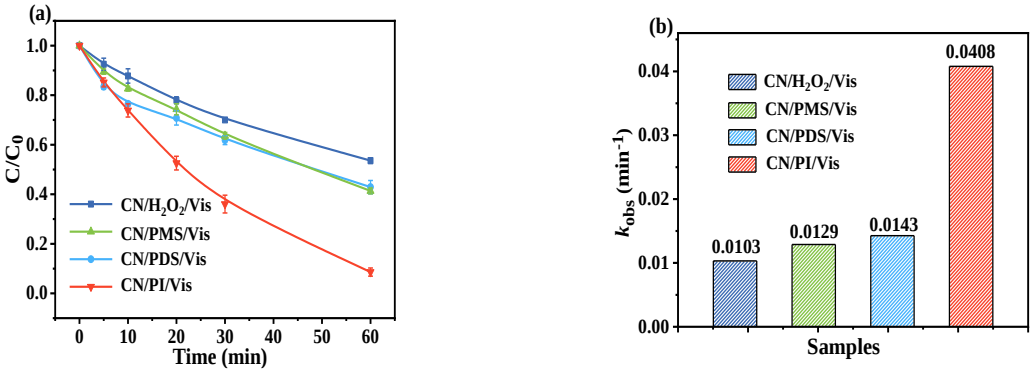

Figure 4. (**a**) Degradation of AO7 and (**b**) removal rate of AO7 in the photocatalytic performance of CN with different oxidants. Experimental conditions: $[AO7]_0$ = 10 ppm, $[CN]_0$ = 0.50 g/L, $[Oxidant]_0$ = 0.25 mM, and initial pH = 5.5.

Table 2. Comparison of the performance of the CN/PI/Vis system with other reported PI−based systems.

Reaction System	Pollutant	Apparent Rate Constants (min^{-1})	Operating Conditions	Ref.
CN/PI/Vis	AO7	0.0408	[catalyst] = 0.5 g/L; [PI] = 0.25 mM; initial pH = 5.50; T = 24 °C	This work
WO_3/PI	4-CP	0.0172	[catalyst] = 0.5 g/L; [PI] = 1 mM; initial pH = 4.0; T = 22 °C	[40]
SBC/PI	DCF	0.0244	[catalyst] = 0.1 g/L; [PI] = 5 mM; initial pH = 6.28; T = 25 °C	[43]
I-GAC/PI	AO7	0.0521	[catalyst] = 1.0 g/L; [PI] = 2.5 mM; initial pH = 5.27	[44]
Fe/Mn-SBC/PI	TCP	0.0257	[catalyst] = 1.0 g/L; [PI] = 5 mM; initial pH = 5.30; T = 25 °C	[45]
N-BWO/PI/Vis	TC	0.0277	[catalyst] = 10 mg; [PI] = 0.1 g/L; initial pH = 7.0; T = 25 °C	[46]
CWBC/PI	SDZ	0.0586	[catalyst] = 0.5 g/L; [PI] = 5 mM; initial pH = 3.0; T = 25 °C	[24]
SBC-700/PI	AO7	0.0279	[catalyst] = 0.4 g/L; [PI] = 1 mM; initial pH = 3.0; T = 25 °C	[47]
ABTS/PI	BPA	0.0352	[catalyst] = 100 μM; [PI] = 1 mM; initial pH = 7.0	[48]

3.3. Mechanism

To gain insight into the fundamental mechanisms of the CN/PI/Vis system, EPR tests and quenching experiments were conducted to identify the involved reactive species. As shown in Figure 5a, the signal of the $^{\bullet}O_2^-$ adduct (DMPO-O_2^-) in the CN/PI/Vis system was enhanced compared to that in the individual PI/Vis process, and the signal peak of $^{\bullet}O_2^-$ was also detected in the CN/Vis system. In contrast, slight $^1O_2$ signals were also observed in the CN/PI/Vis, PI/Vis, and CN/Vis systems, respectively (Figure 5b). Moreover, the $^1O_2$ signal was stronger in the PI/Vis system than in the CN/Vis system, indicating that the production of $^1O_2$ for AO7 removal mainly originates from the photoactivation of PI. As presented in Figure 5c, no signals of DMPO-$IO_3^{\bullet}$ and DMPO-$^{\bullet}$OH were found in the CN/PI/Vis system, ruling out the existence of them in the reaction.

To further determine the involvement of reactive species $^{\bullet}O_2^-$ and $^1O_2$, quenching experiments were conducted. *p*-BQ and L-Histidine serve as typical scavengers for $^{\bullet}O_2^-$ and $^1O_2$, respectively [49]. As depicted in Figure 5d, the addition of 5 mM *p*-BQ and 5 mM L-Histidine resulted in similar inhibitory effects, with the degradation efficiency of AO7 decreasing from 92.3% to 20%, confirming that both $^{\bullet}O_2^-$ and $^1O_2$ contribute to the oxidative degradation of AO7.

A plausible degradation mechanism for the CN/PI/Vis system was hypothesized based on the aforementioned results. At first, it was assumed that the reactive oxygen species might be produced via the photoactivation of a photosensitive catalyst. The energy transfer to O_2 ($^3\sum_{g-}$) from the excited state of a sensitizer, formed by light absorption, led to the generation of excited state $^1O_2$ ($^1\Delta_g$) (Equation (7)) [50]. On the one hand, the photocatalyst CN can generate electrons and holes (Equation (8)) when it is excited by light irradiation. The photo-induced electrons in the conduction band can convert IO_4^- to IO_3^- via Equation (9) [51]. On the other hand, when IO_4^- is activated by light energy, e− and $IO_4^{\bullet}$ are produced in the system (Equation (10)) [52]. Dissolved oxygen (DO) tends to obtain an electron form $^{\bullet}O_2^-$ (Equation (11)). Additionally, IO_4^- can react further with $^{\bullet}O_2^-$ to generate $^1O_2$ (Equation (12)), thereby significantly accelerating the oxidation reaction. Based on these results and analyses, the plausible mechanism of AO7 degradation by the CN/PI/Vis system is illustrated in Figure 6.

$$\text{light} + \text{CN}\ (^3\textstyle\sum_g{}^-) + O_2 \rightarrow {}^1O_2\ (^1\Delta_g) \quad (7)$$

$$\text{CN} + \text{light} \rightarrow h_{VB}{}^+ + e_{CB}{}^- \quad (8)$$

$$H_2O + 2e^- + IO_4{}^- \rightarrow 2OH^- + IO_3{}^- \quad (9)$$

$$IO_4{}^- + \text{Vis} \rightarrow IO_4{}^{\bullet} + e^- \quad (10)$$

$$O_2 + e^- \rightarrow {}^{\bullet}O_2{}^- \quad (11)$$

$$IO_4^- + 2^{\bullet}O_2^- + H_2O \rightarrow IO_3^- + 2\,{}^1O_2 + 2OH^- \quad (12)$$

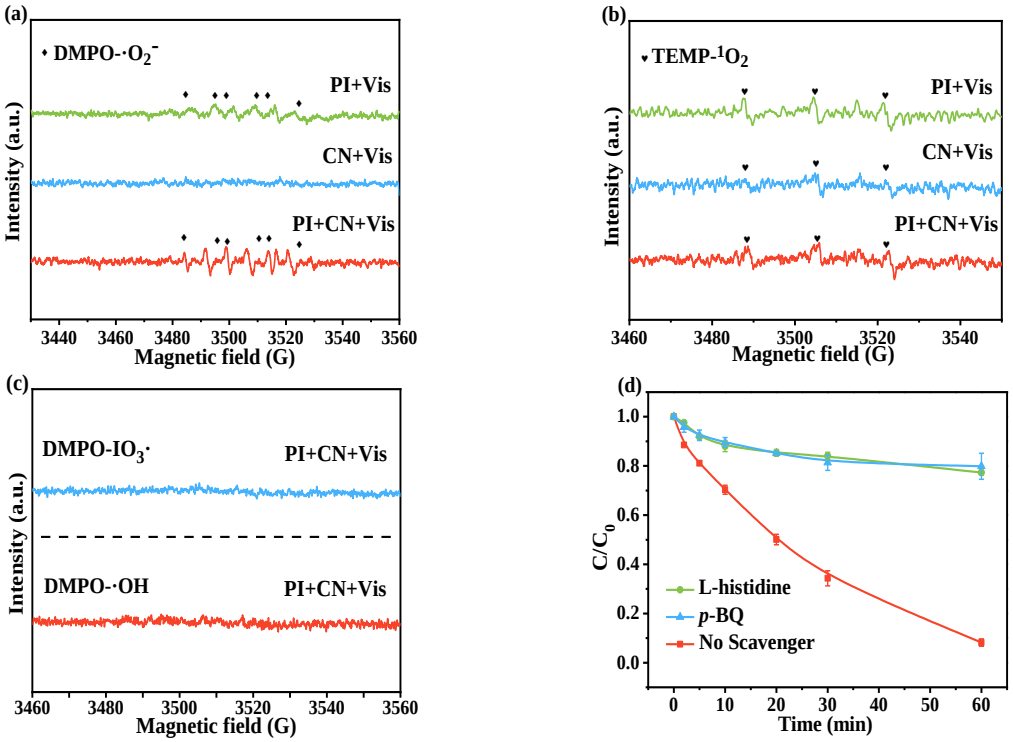

Figure 5. EPR spectra of (**a**) $^{\bullet}O_2^-$ (in anhydrous methanol); (**b**) $^1O_2$ (in ultrapure water), and (**c**) $IO_3^{\bullet}$ (in DMSO)/$^{\bullet}OH$ (in ultrapure water) in different systems. (**d**) The effect of radical scavengers on the removal of AO7 in the CN/PI/Vis system. Experimental conditions: $[AO7]_0$ = 10 ppm, $[CN]_0$ = 0.50 g/L, $[PI]_0$ = 0.25 mM, and initial pH = 5.5.

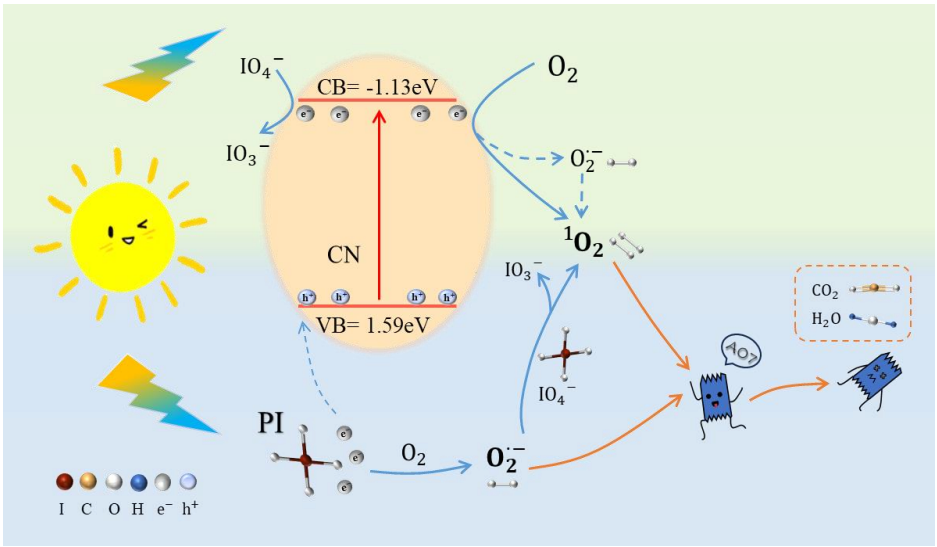

Figure 6. Possible mechanism for the photodegradation of AO7 under the CN/PI/Vis system.

3.4. Impacts of Operating Parameters

The effects of catalyst dosage, PI concentration, and solution pH are thoroughly investigated in Figure 7. The degradation efficiency of AO7 in the CN/PI/Vis system was investigated at various CN dosages, ranging from 0.10 to 0.75 g/L. As observed in Figure 7a, the k_{obs} value increased from 0.0126 to 0.0404 min^{-1} as the CN dosage was raised from 0.10 to 0.50 g/L. Increasing the dosage of CN is expected to provide more active sites for PI

adsorption and activation, as well as more electrons and holes under the irradiation of light. However, increasing the CN dosage from 0.50 to 0.75 g/L did not significantly enhance the removal efficiency, likely because the incident visible light is blocked and scattered by excessively suspended particles, resulting in less light reaching the catalyst [53,54]. From an economic perspective, a catalyst dose of 0.50 g/L was used for subsequent experiments. Figure 7b depicts the impact of PI concentration on AO7 removal. The concentration of PI was positively correlated with the rate of AO7 degradation. As the PI concentration increased from 0.05 mM to 0.25 mM, the AO7 removal efficiency was promoted accordingly, and the rate constant of AO7 removal increased from 0.0226 to 0.0404 min^{-1}. As the amount of PI increased to 0.50 mM, the k_{obs} decreased slightly to 0.0399 min^{-1}, which might be due to competitive reactions between excessive PI and the target contaminant with the reactive species [37]. This result indicates that, within a certain range, the increasing concentration of PI can effectively accept photo-induced electrons, improving the oxidation performance of the entire system. Therefore, 0.25 mM was selected as an optimal PI dosage and applied for subsequent degradation reactions.

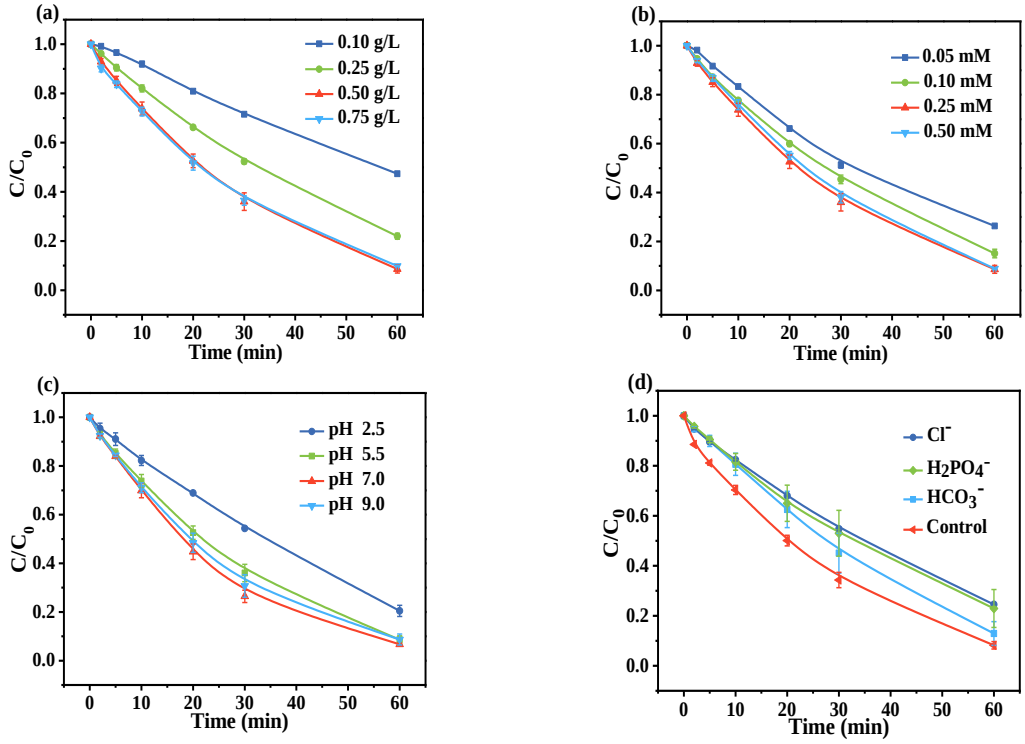

Figure 7. Effects of (**a**) CN dosage, (**b**) PI concentration, (**c**) initial pH, and (**d**) inorganic anions on AO7 removal in the CN/PI/Vis system. Except for the parameter being tested, other experimental conditions were fixed: $[AO7]_0$ = 10 ppm, $[CN]_0$ = 0.50 g/L, $[PI]_0$ = 0.25 mM, initial pH = 5.5, and $[ions]_0$ = 5 mM.

Reaction pH is crucial for decomposing peroxides to form reactive species. The initial pH was adjusted to 2.5, 5.5, 7.0, and 9.0 to explore its effect on AO7 elimination. The initial pH of the AO7 solution was approximately 5.5, as shown in Figure 7c. When it was reduced to 2.5, AO7 removal decreased by ~10%. AO7 (pK_a = 1) always has a negatively charged sulfonic group in the pH range investigated [55]. In contrast, the pH_{pzc} of CN lies between 4~5 and it tends to be positively charged when the pH of the solution is below 4.0 [23], which seems to imply that the enhanced adsorption of AO7 by the catalyst is due to the effect of electrostatic attraction. However, previous studies have reported that the photo-induced electrons on the surface of CN tend to react with H^+ in solution (Equation (13)), and the conversion of $IO_3^{\bullet}$ to IO_4^- also increases with decreasing pH (Equation (14)) [56]. This results in a slight decrease in the removal of AO7 under acidic conditions (i.e., pH 2.5). When the pH is increased from 5.5 to 9, AO7 degradation efficiency

remains stable, demonstrating the good oxidation performance of the CN/PI/Vis system over a wide pH range.

$$e_{aq}^{-} + H^{+} \rightarrow H^{\bullet} \quad (13)$$

$$IO_3^{\bullet} + H^{\bullet} \rightarrow IO_3^{-} + H^{+} \quad (14)$$

3.5. Effects of Coexisting Anions

Given the ubiquity of inorganic anions in natural water, this study investigated their interference with AO7 degradation in the CN/PI/Vis system. As shown in Figure 7d, the presence of Cl^{-}, HCO_3^{-}, and $H_2PO_4^{-}$ anions slightly inhibited the degradation of AO7, likely due to the following aspects. On the one hand, the anions may form an inorganic layer on the catalyst's surface, partially blocking the active sites [57]. On the other hand, the anions could compete with AO7 for reactive oxidative species, thereby inhibiting the oxidation ability of the system [58]. Specifically, HCO_3^{-} (or CO_3^{2-}) and $H_2PO_4^{-}$ anions might be adsorbed on the catalyst surface, impeding the mass transfer of oxidants and pollutants, thereby inhibiting the oxidation reaction. Additionally, Cl^{-} and CO_3^{2-} can react with reactive species, forming less reactive chlorine species ($Cl^{\bullet}$ and $Cl_2^{\bullet-}$) and carbonate radicals, respectively. This reduces the system's oxidizing capacity and decreases the elimination efficiency of AO7 [59].

3.6. Stability and Reuse of Catalysts

Stability and recyclability are critical for the effective use of catalysts in real water. Therefore, this study conducted cyclic experiments on the CN material. As shown in Figure 8, after three cycles, CN still maintains acceptable efficiency for AO7 removal, though a slight decrease was observed, indicating its relative stability in the oxidation process. The decreased removal efficiency after the third cycle might be ascribed to the adsorption of AO7 and its degradation products on the catalyst surface, which covers a significant portion of the active sites [60].

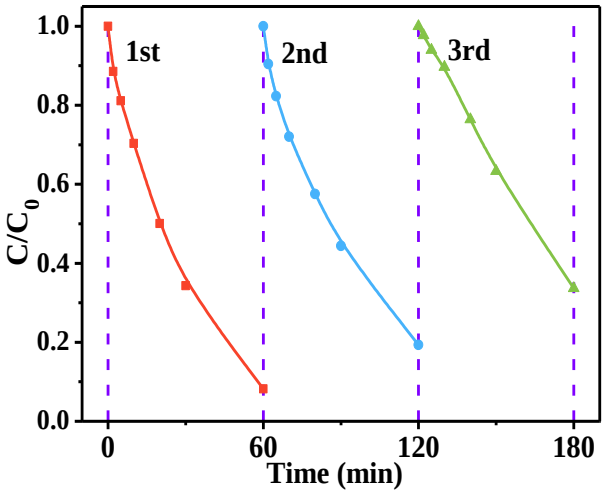

Figure 8. Stability test of CN. Experimental conditions: $[AO7]_0$ = 10 ppm, $[CN]_0$ = 0.5g/L, $[PI]_0$ = 0.25 mM, initial pH = 5.5.

To analyze the change of surface physicochemical properties of catalyst, the used catalyst was then characterized using XRD and XPS. The XRD (Figure 9a) pattern shows that the catalyst's crystal phase has not changed significantly before and after the reaction. XPS (Figure 9b–d) analysis was conducted to determine the surface composition of CN, revealing that it consists of C and N species. The C 1s narrow spectrum displayed three peaks at 288.1, 286.2, and 284.8 eV, corresponding to sp^2 hybridized carbon (N=C-N), sp^3 coordinated carbon (C-N), and sp^2 C-C bonds, respectively. The N 1s spectrum features three characteristic peaks at 401.1 eV, 400.1 eV, and 398.6 eV, corresponding to the terminal

amino functional group (C-NH_2), sp^2 hybridized nitrogen (C-N=C), and tertiary nitrogen (N-C_3), respectively. Compared with the used CN sample, the proportions of C-NH_2 and C-N=C decreased from 6.9% and 19.0% to 6.5% and 16.7%, respectively, whereas the proportion of N-C_3 increased from 74.1% to 76.9%. According to previous research, carbonous material with more C-N structures indicates that the structure of triazine units becomes more ordered [61]. Compared to the fresh CN (6.7%), the proportion of the C-N peak in the used sample remained relatively stable (6.3%), indicating that the surface properties of the catalyst are stable before and after the reaction, which is conducive to the catalyst's reuse.

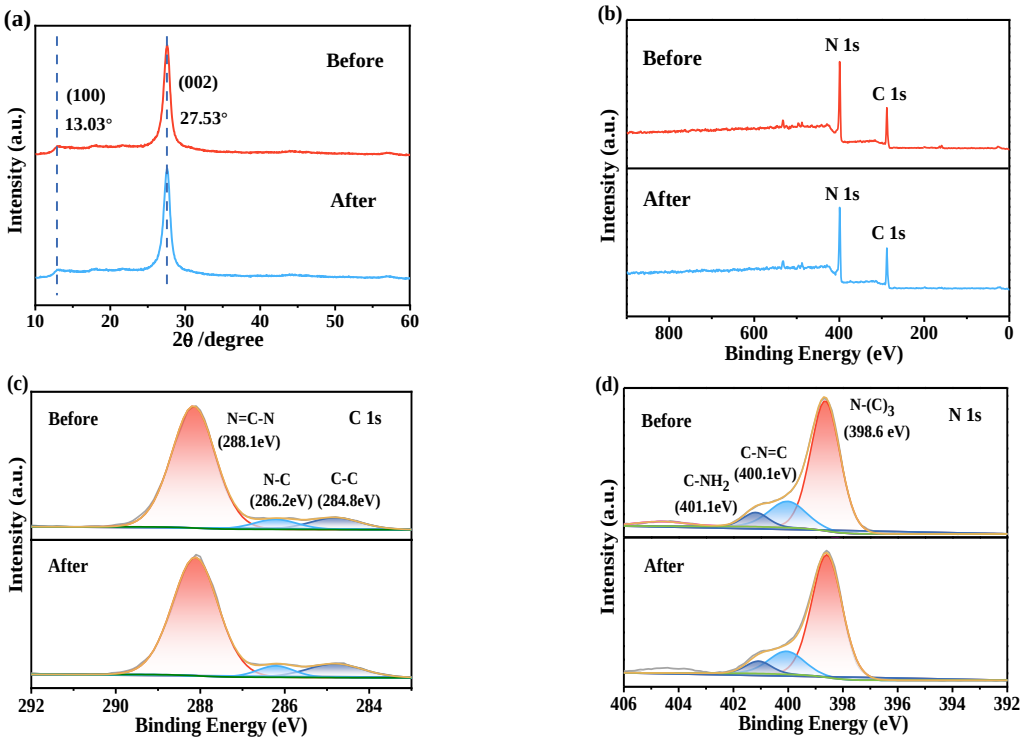

Figure 9. Stability and recyclability of CN: (**a**) XRD patterns, XPS spectra of (**b**) a survey scan, (**c**) C 1s, and (**d**) N 1s before and after the reaction.

4. Conclusions

This paper reports the preparation of a highly efficient carbon nitride catalyst using melamine as a precursor. It can effectively activate PI to eliminate organic pollutants in the presence of visible light. With the addition of 0.25 mM PI to the CN/Vis system, 92.3% of AO7 was efficiently removed within 60 min. Importantly, the heterogeneous photocatalytic PI system exhibits better oxidation performance compared to systems based on PMS, PDS, and H_2O_2, respectively. Based on a variety of experiments and characterizations, $^1O_2$ and $^{\bullet}O_2^-$ were revealed as the dominant reactive species for the degradation of pollutants. Additionally, the CN demonstrated good stability during the reaction, with excellent anti-interference capabilities. In brief, heterogeneous photocatalytic PI activation has been proven to be an efficient and eco-friendly technology for wastewater treatment.

Author Contributions: Conceptualization, Y.X.; methodology, W.X.; software, W.X. and Q.W.; validation, W.X.; formal analysis, W.X. and J.H.; investigation, W.X. and J.H.; resources, F.L. and Y.X.; data curation, W.X.; writing—original draft preparation, W.X., X.Y. and Y.X.; writing—review and editing, W.X. and Y.X.; visualization, W.X. and Q.W.; supervision, F.L. and Y.X.; project administration, F.L. and Y.X.; funding acquisition, F.L. All authors have read and agreed to the published version of the manuscript.

Funding: This study was funded by the Hubei Provincial Natural Science Foundation of China (Grant No. 2022CFB986) and the Open Foundation of the Hubei Key Laboratory of Regional Development and Environmental Response, China (2021(A) 003).

Data Availability Statement: The data presented in this study are available on request from the corresponding author.

Conflicts of Interest: The authors declare no conflicts of interest.

References

1. Mahbub, P.; Duke, M. Scalability of advanced oxidation processes (AOPs) in industrial applications: A review. *J. Environ. Manag.* **2023**, *345*, 118861. [CrossRef] [PubMed]
2. Tan, J.; Tian, N.; Li, Z.; Li, J.; Yao, X.; Vakili, M.; Lu, Y.; Zhang, T. Intrinsic defect engineering in graphitic carbon nitride for photocatalytic environmental purification: A review to fill existing knowledge gaps. *Chem. Eng. J.* **2021**, *421*, 127729. [CrossRef]
3. Subodh; Prakash, K.; Chaudhary, K.; Masram, D.T. A new triazine-cored covalent organic polymer for catalytic applications. *Appl. Catal. A Gen.* **2020**, *593*, 117411. [CrossRef]
4. Wu, N.; Zhao, B.; Liu, J.; Li, Y.; Chen, Y.; Chen, L.; Wang, M.; Guo, Z. MOF-derived porous hollow Ni/C composites with optimized impedance matching as lightweight microwave absorption materials. *Adv. Compos. Hybrid Mater.* **2021**, *4*, 707–715. [CrossRef]
5. Ghanbari, F.; Zirrahi, F.; Lin, K.-Y.A.; Kakavandi, B.; Hassani, A. Enhanced electro-peroxone using ultrasound irradiation for the degradation of organic compounds: A comparative study. *J. Environ. Chem. Eng.* **2020**, *8*, 104167. [CrossRef]
6. Hu, P.; Long, M. Cobalt-catalyzed sulfate radical-based advanced oxidation: A review on heterogeneous catalysts and applications. *Appl. Catal. B Environ.* **2016**, *181*, 103–117. [CrossRef]
7. Hu, J.; Zou, Y.; Li, Y.; Yu, Z.; Bao, Y.; Lin, L.; Li, B.; Li, X.-Y. Periodate activation by atomically dispersed Mn on carbon nanotubes for the production of iodate radicals and rapid degradation of sulfadiazine. *Chem. Eng. J.* **2023**, *472*, 144862. [CrossRef]
8. Gong, J.; Jiang, H.; Li, X.; Cheng, H.; Wang, Z.; Cai, J.; Li, M.; Wang, P.; Wang, H.; Hu, X.; et al. Highly efficient activation of periodate by a manganese-modified biochar to rapidly degrade methylene blue. *Environ. Res.* **2024**, *241*, 117657. [CrossRef]
9. Zong, Y.; Zhang, H.; Shao, Y.; Ji, W.; Zeng, Y.; Xu, L.; Wu, D. Surface-mediated periodate activation by nano zero-valent iron for the enhanced abatement of organic contaminants. *J. Hazard. Mater.* **2023**, *423*, 126991. [CrossRef]
10. Lee, Y.C.; Chen, M.J.; Huang, C.P.; Kuo, J.; Lo, S.L. Efficient sonochemical degradation of perfluorooctanoic acid using periodate. *Ultrason. Sonochem.* **2016**, *31*, 499–505. [CrossRef]
11. Choi, Y.; Yoon, H.I.; Lee, C.; Vetrakova, L.; Heger, D.; Kim, K.; Kim, J. Activation of Periodate by Freezing for the Degradation of Aqueous Organic Pollutants. *Environ. Sci. Technol.* **2018**, *52*, 5378–5385. [CrossRef] [PubMed]
12. Bokare, A.D.; Choi, W. Singlet-Oxygen Generation in Alkaline Periodate Solution. *Environ. Sci. Technol.* **2015**, *49*, 14392–14400. [CrossRef] [PubMed]
13. Sun, H.; He, F.; Choi, W. Production of Reactive Oxygen Species by the Reaction of Periodate and Hydroxylamine for Rapid Removal of Organic Pollutants and Waterborne Bacteria. *Environ. Sci Technol.* **2020**, *54*, 6427–6437. [CrossRef] [PubMed]
14. Deng, Y.; Li, B.; Zhang, T. Bacteria That Make a Meal of Sulfonamide Antibiotics: Blind Spots and Emerging Opportunities. *Environ. Sci. Technol.* **2018**, *52*, 3854–3868. [CrossRef]
15. Li, X.; Liu, X.; Qi, C.; Lin, C. Activation of periodate by granular activated carbon for acid orange 7 decolorization. *J. Taiwan Inst. Chem. Eng.* **2016**, *68*, 211–217. [CrossRef]
16. Li, R.; Wang, J.; Wu, H.; Zhu, Z.; Guo, H. Periodate activation for degradation of organic contaminants processes, performance and mechanism. *Sep. Purif. Technol.* **2022**, *292*, 120928. [CrossRef]
17. Védrine, J.C. Metal Oxides in Heterogeneous Oxidation Catalysis: State of the Art and Challenges for a More Sustainable World. *ChemSusChem* **2019**, *12*, 577–588. [CrossRef]
18. Van Velthoven, N.; Wang, Y.; Van Hees, H.; Henrion, M.; Bugaev, A.L.; Gracy, G.; Amro, K.; Soldatov, A.V.; Alauzun, J.G.; Mutin, P.H.; et al. Heterogeneous Single-Site Catalysts for C–H Activation Reactions: Pd(II)-Loaded S,O-Functionalized Metal Oxide-Bisphosphonates. *ACS Appl. Mater. Interfaces* **2020**, *12*, 47457–47466. [CrossRef]
19. Xu, C.; Yang, G.; Li, J.; Zhang, S.; Fang, Y.; Peng, F.; Zhang, S.; Qiu, R. Efficient purification of tetracycline wastewater by activated persulfate with heterogeneous Co-V bimetallic oxides. *J. Colloid Interface Sci.* **2022**, *619*, 188–197. [CrossRef]
20. Zeng, T.; Yu, M.; Zhang, H.; He, Z.; Zhang, X.; Chen, J.; Song, S. In situ synthesis of cobalt ferrites-embedded hollow N-doped carbon as an outstanding catalyst for elimination of organic pollutants. *Sci. Total Environ.* **2017**, *593–594*, 286–296. [CrossRef]
21. Meng, Y.; Li, Z.; Tan, J.; Li, J.; Wu, J.; Zhang, T.; Wang, X. Oxygen-doped porous graphitic carbon nitride in photocatalytic peroxymonosulfate activation for enhanced carbamazepine removal: Performance, influence factors and mechanisms. *Chem. Eng. J.* **2022**, *429*, 130860. [CrossRef]
22. Long, Y.; Dai, J.; Zhao, S.; Huang, S.; Zhang, Z. Metal–organic framework-derived magnetic carbon for efficient decontamination of organic pollutants via periodate activation: Surface atomic structure and mechanistic considerations. *J. Hazard. Mater.* **2022**, *424*, 126786. [CrossRef] [PubMed]

23. Chen, Y.; Yuan, X.; Jiang, L.; Zhao, Y.; Chen, H.; Shangguan, Z.; Qin, C.; Wang, H. Insights into periodate oxidation of antibiotics mediated by visible-light-induced polymeric carbon nitride: Performance and mechanism. *Chem. Eng. J.* **2023**, *457*, 141147. [CrossRef]
24. He, L.; Yang, C.; Ding, J.; Lu, M.-Y.; Chen, C.-X.; Wang, G.-Y.; Jiang, J.-Q.; Ding, L.; Liu, G.-S.; Ren, N.-Q.; et al. Fe, N-doped carbonaceous catalyst activating periodate for micropollutant removal: Significant role of electron transfer. *Appl. Catal. B Environ.* **2022**, *303*, 120880. [CrossRef]
25. Gogoi, D.; Shah, A.K.; Qureshi, M.; Golder, A.K.; Peela, N.R. Silver grafted graphitic-carbon nitride ternary hetero-junction Ag/gC_3N_4(Urea)-gC_3N_4(Thiourea) with efficient charge transfer for enhanced visible-light photocatalytic green H_2 production. *Appl. Surf. Sci.* **2021**, *558*, 149900. [CrossRef]
26. Chen, F.; Liu, L.L.; Chen, J.J.; Li, W.W.; Chen, Y.P.; Zhang, Y.J.; Wu, J.H.; Mei, S.C.; Yang, Q.; Yu, H.Q. Efficient decontamination of organic pollutants under high salinity conditions by a nonradical peroxymonosulfate activation system. *Water Res.* **2021**, *191*, 116799. [CrossRef]
27. Wang, Y.; Du, P.; Pan, H.; Fu, L.; Zhang, Y.; Chen, J.; Du, Y.; Tang, N.; Liu, G. Increasing Solar Absorption of Atomically Thin 2D Carbon Nitride Sheets for Enhanced Visible-Light Photocatalysis. *Adv Mater.* **2019**, *31*, 1807540. [CrossRef]
28. Chen, F.; Liu, L.L.; Wu, J.H.; Rui, X.H.; Chen, J.J.; Yu, Y. Single-Atom Iron Anchored Tubular g-C(3) N(4) Catalysts for Ultrafast Fenton-Like Reaction: Roles of High-Valency Iron-Oxo Species and Organic Radicals. *Adv Mater.* **2022**, *34*, 2202891. [CrossRef]
29. Prakash, K.; Kumar, P.S.; Pandiaraj, S.; Karuthapandian, S. Versatile, metal free and temperature-controlled g-C_3N_4 as a highly efficient and robust photocatalyst for the degradation of organic pollutants. *Res. Chem. Intermed.* **2018**, *45*, 1147–1167. [CrossRef]
30. Jiang, X.; Li, J.; Fang, J.; Gao, L.; Cai, W.; Li, X.; Xu, A.; Ruan, X. The photocatalytic performance of g-C_3N_4 from melamine hydrochloride for dyes degradation with peroxymonosulfate. *J. Photochem. Photobiol. A Chem.* **2017**, *336*, 54–62. [CrossRef]
31. Sun, P.; Xiong, J.; Sun, P.; Fang, Y.; Liu, H.; Liu, H.; Xiong, B.; Wang, H.; Li, X.A. Additional O doping significantly improved the catalytic performance of Mn/O co-doped g-C_3N_4 for activating periodate and degrading organic pollutants. *Sep. Purif. Technol.* **2024**, *331*, 125593. [CrossRef]
32. Wang, Q.; Zeng, H.; Liang, Y.; Cao, Y.; Xiao, Y.; Ma, J. Degradation of bisphenol AF in water by periodate activation with FeS (mackinawite) and the role of sulfur species in the generation of sulfate radicals. *Chem. Eng. J.* **2021**, *407*, 126738. [CrossRef]
33. Liu, W.; Li, Y.; Liu, F.; Jiang, W.; Zhang, D.; Liang, J. Visible-light-driven photocatalytic degradation of diclofenac by carbon quantum dots modified porous g-C(3)N(4): Mechanisms, degradation pathway and DFT calculation. *Water Res.* **2019**, *150*, 431–441. [CrossRef] [PubMed]
34. Li, R.; Hu, H.; Ma, Y.; Liu, X.; Zhang, L.; Zhou, S.; Deng, B.; Lin, H.; Zhang, H. Persulfate enhanced photocatalytic degradation of bisphenol A over wasted batteries-derived $ZnFe_2O_4$ under visible light. *J. Clean. Prod.* **2020**, *276*, 124246. [CrossRef]
35. Xu, Y.; Tang, X.; Xiao, Y.; Tang, H.; Lin, H.; Lv, Y.; Zhang, H. Persulfate promoted visible photocatalytic elimination of bisphenol A by g-C(3)N(4)-CeO(2) S-scheme heterojunction: The dominant role of photo-induced holes. *Chemosphere* **2023**, *331*, 138765. [CrossRef]
36. Tang, H.; Li, R.; Fan, X.; Xu, Y.; Lin, H.; Zhang, H. A novel S-scheme heterojunction in spent battery-derived $ZnFe_2O_4$/g-C_3N_4 photocatalyst for enhancing peroxymonosulfate activation and visible light degradation of organic pollutant. *J. Environ. Chem. Eng.* **2022**, *10*, 107797. [CrossRef]
37. Sun, Y.-J.; Fang, Z.-Y.; Huang, X.-T.; Bai, C.-W.; Zhu, K.-A.; Chen, X.-J.; Zhang, B.-B.; Zhang, Y.-S.; Yang, Q.; Zheng, J.-X.; et al. Efficient photo-switchable activation of periodate by nitrogen-vacancy-rich carbon nitride for organic contaminant removal: Theoretical predictions and experimental validations. *Appl. Catal. B Environ.* **2023**, *337*, 122994. [CrossRef]
38. Wang, X.; Tang, W.; Jiang, L.; Feng, J.; Yang, J.; Zhou, S.; Li, W.; Yuan, X.; Wang, H.; Wang, J.; et al. Mechanism insights into visible light-induced crystalline carbon nitride activating periodate for highly efficient ciprofloxacin removal. *Chem. Eng. J.* **2023**, *471*, 144521. [CrossRef]
39. Wu, M.; He, X.; Jing, B.; Wang, T.; Wang, C.; Qin, Y.; Ao, Z.; Wang, S.; An, T. Novel carbon and defects co-modified g-C(3)N(4) for highly efficient photocatalytic degradation of bisphenol A under visible light. *J. Hazard. Mater.* **2020**, *384*, 121323. [CrossRef]
40. Kim, H.; Yoo, H.-Y.; Hong, S.; Lee, S.; Lee, S.; Park, B.-S.; Park, H.; Lee, C.; Lee, J. Effects of inorganic oxidants on kinetics and mechanisms of WO_3-mediated photocatalytic degradation. *Appl. Catal. B.* **2015**, *162*, 515–523. [CrossRef]
41. Lee, Y.; Lee, S.; Cui, M.; Ren, Y.; Park, B.; Ma, J.; Han, Z.; Khim, J. Activation of peroxodisulfate and peroxymonosulfate by ultrasound with different frequencies: Impact on ibuprofen removal efficient, cost estimation and energy analysis. *Chem. Eng. J.* **2021**, *413*, 127487. [CrossRef]
42. Levason, W. The coordination chemistry of periodate and tellurate ligands. *Coord. Chem. Rev.* **1997**, *161*, 33–79. [CrossRef]
43. He, L.; Yang, S.; Shen, S.; Ma, Y.; Chen, Y.; Xue, J.; Wang, J.; Zheng, L.; Wu, L.; Zhang, Z.; et al. Novel insights into the mechanism of periodate activation by heterogeneous ultrasonic-enhanced sludge biochar: Relevance for efficient degradation of levofloxacin. *J. Hazard. Mater.* **2022**, *434*, 128860. [CrossRef]
44. Li, X.; Liu, X.; Lin, C.; Qi, C.; Zhang, H.; Ma, J. Enhanced activation of periodate by iodine-doped granular activated carbon for organic contaminant degradation. *Chemosphere* **2017**, *181*, 609–618. [CrossRef] [PubMed]
45. He, L.; Shi, Y.; Chen, Y.; Shen, S.; Xue, J.; Ma, Y.; Zheng, L.; Wu, L.; Zhang, Z.; Yang, L. Iron-manganese oxide loaded sludge biochar as a novel periodate activator for thiacloprid efficient degradation over a wide pH range. *Sep. Purif. Technol.* **2022**, *288*, 120703. [CrossRef]

46. Niu, J.; Zhou, Y.; He, W.; Xiao, Y.; Song, X.; Zeng, X.; Huang, G.; Feng, D.; Liang, B.; Zhang, J. The controllable oxygen vacancies in N doped Bi_2WO_{6-x} for periodate activation: The synergy of superoxide and iodate radical. *J. Water Process Eng.* **2024**, *64*, 105747. [CrossRef]
47. Xiao, P.; Yi, X.; Wu, M.; Wang, X.; Zhu, S.; Gao, B.; Liu, Y.; Zhou, H. Catalytic performance and periodate activation mechanism of anaerobic sewage sludge-derived biochar. *J Hazard Mater* **2022**, *424*, 127692. [CrossRef]
48. Guo, X.; Yang, F.; Deng, S.; Ding, Y. Activation of periodate by ABTS as an electron shuttle for degradation of aqueous organic pollutants and enhancement effect of phosphate. *Chemosphere* **2024**, *349*, 140793. [CrossRef]
49. Lei, Y.; Yu, Y.; Lei, X.; Liang, X.; Cheng, S.; Ouyang, G.; Yang, X. Assessing the Use of Probes and Quenchers for Understanding the Reactive Species in Advanced Oxidation Processes. *Environ. Sci. Technol.* **2023**, *57*, 5433–5444. [CrossRef]
50. Bianco, G.V.; Sacchetti, A.; Grande, M.; D'orazio, A.; Milella, A.; Bruno, G. Effective hole conductivity in nitrogen-doped CVD-graphene by singlet oxygen treatment under photoactivation conditions. *Sci. Rep.* **2022**, *12*, 8703. [CrossRef]
51. Wu, Y.; Tan, X.; Zhao, J.; Ma, J. alpha-Fe(2)O(3) mediated periodate activation for selective degradation of phenolic compounds via electron transfer pathway under visible irradiation. *J. Hazard. Mater.* **2023**, *454*, 131506. [CrossRef] [PubMed]
52. Song, T.; Gao, Y.; Yu, X.; Su, R.; Deng, Q.; Wang, Z. Advances in photo-mediated advanced oxidation of periodate toward organics degradation. *J. Water Process Eng.* **2024**, *61*, 105261. [CrossRef]
53. Sun, H.; Guo, F.; Pan, J.; Huang, W.; Wang, K.; Shi, W. One-pot thermal polymerization route to prepare N-deficient modified g-C_3N_4 for the degradation of tetracycline by the synergistic effect of photocatalysis and persulfate-based advanced oxidation process. *Chem. Eng. J.* **2021**, *406*, 126844. [CrossRef]
54. Yang, J.; Zhu, M.; Dionysiou, D.D. What is the role of light in persulfate-based advanced oxidation for water treatment? *Water Res.* **2021**, *189*, 116627. [CrossRef]
55. Long, Y.; Li, S.; Yang, P.; Chen, X.; Liu, W.; Zhan, X.; Xue, C.; Liu, D.; Huang, W. Synthesis of ZIF-67 derived honeycomb porous Co/NC catalyst for AO7 degradation via activation of peroxymonosulfate. *Sep. Purif. Technol.* **2022**, *286*, 120470. [CrossRef]
56. Santos, V.P.; Pereira, M.F.R.; Faria, P.C.C.; Órfão, J.J.M. Decolourisation of dye solutions by oxidation with H_2O_2 in the presence of modified activated carbons. *J. Hazard. Mater.* **2009**, *162*, 736–742. [CrossRef]
57. Guillard, C.; Puzenat, E.; Lachheb, H.; Houas, A.; Herrmann, J.M. Why inorganic salts decrease the TiO_2 photocatalytic efficiency. *J. Alloys Compd.* **2007**, *503*, 485–489. [CrossRef]
58. Xu, L.; Ye, Z.; Pan, Y.; Zhang, Y.; Gong, H.; Mei, X.; Qiao, W.; Gan, L. Effect of lignocellulosic biomass composition on the performance of biochar for the activation of peroxymonosulfate to degrade diclofenac. *Sep. Purif. Technol.* **2023**, *311*, 123312. [CrossRef]
59. Guo, W.; Zhao, Q.; Du, J.; Wang, H.; Li, X.; Ren, N. Enhanced removal of sulfadiazine by sulfidated ZVI activated persulfate process: Performance, mechanisms and degradation pathways. *Chem. Eng. J.* **2020**, *388*, 124303. [CrossRef]
60. Long, Y.; Bu, S.; Huang, Y.; Shao, Y.; Xiao, L.; Shi, X. N-doped hierarchically porous carbon for highly efficient metal-free catalytic activation of peroxymonosulfate in water: A non-radical mechanism. *Chemosphere* **2019**, *216*, 545–555. [CrossRef]
61. Chen, B.; Liu, X.; Liu, B.; Han, Q.; Li, L.; Wang, L.; Shu, Y.; Zang, L.; Zhu, W.; Wang, Z. Singlet oxygen generation in light-assisted peroxymonosulfate activation by carbon nitride: Role of elevated crystallinity. *Chemosphere* **2023**, *321*, 138112. [CrossRef] [PubMed]